

We are IntechOpen, the world's leading publisher of Open Access books Built by scientists, for scientists

6,900

Open access books available

185,000

International authors and editors

200M

Downloads

Our authors are among the

154

Countries delivered to

TOP 1%

most cited scientists

12.2%

Contributors from top 500 universities



WEB OF SCIENCE™

Selection of our books indexed in the Book Citation Index
in Web of Science™ Core Collection (BKCI)

Interested in publishing with us?
Contact book.department@intechopen.com

Numbers displayed above are based on latest data collected.
For more information visit www.intechopen.com



Application of Ultrasonics on Preparation of Magnesium Alloys

Xingrui Chen and Qichi Le

Abstract

This chapter mainly describes the application of ultrasonic on preparation of magnesium alloys, which includes all of the interesting and novel research results of authors in the past decade. The chapter includes the following topics to readers: the ultrasonic cavitation behavior in magnesium alloys; the effect of ultrasonic treatment on melt structure; ultrasonic degassing of magnesium alloys; effect of ultrasonic melt treatment on microstructure of magnesium alloys; dual-frequency ultrasonic treatment on solidification of magnesium alloys; and ultrasonic direct-chill (DC) casting process of magnesium alloys billets, including the novel variable-frequency ultrasonic technology. The chapter almost covers all the aspects of ultrasonic application on preparation of magnesium alloys and can help readers have a systematic understanding of ultrasonic melt treatment on magnesium alloys.

Keywords: ultrasonics, magnesium alloy, melt treatment, casting, degassing

1. Introduction

Magnesium alloy is the lightest metal structure material until now. It has caught a lot of attentions from industrial manufacturers all over the world. It is used in many fields such as vehicles, aircrafts, and military industry, due to its great advantages including low density, high strength/weight ratio, etc. [1, 2], while the unique crystal structure, the existence of microporosity, and coarse microstructure limit its application and development. To solve these problems, researchers have developed some technologies. For example, the semisolid process technology [3] and rapid solidification technology [4] can refine the Mg grain, and the argon degassing technology can remove the hydrogen from the melt. However, the ultrasonic melt treatment technology is a best choice considering its environmental friendly and easy realized characteristics.

After decades of development, this technology has been employed in many aspects for preparation of magnesium alloy. This chapter is aimed at introducing the role of ultrasound on metallurgy process of magnesium alloys. We hope people who are interested in this field may be inspired by this chapter.

2. Ultrasonic cavitation in magnesium alloy

The reason why ultrasonic melt treatment technology attracts many researchers is that it has excellent ability to refine the microstructure of alloys. This

improvement is identified as the contribution of ultrasonic cavitation. In other words, the cavitation holes the key to ultrasonic refinement. Therefore, it is of great importance to investigate the cavitation behavior in magnesium alloy. However, because of the fact that the characteristics of magnesium melt such as high temperature and opacity, the numerical simulation is a viable method to reflect the cavitation behavior.

The cavitation behavior in magnesium melt is calculated the Rayleigh–Plesset Equation [5]:

$$R \left(\frac{d^2 R}{dt^2} \right) + \frac{3}{2} \left(\frac{dR}{dt} \right)^2 = \frac{1}{\rho} \left[\left(P_0 + \frac{2\sigma}{R_0} \right) \left(\frac{R_0}{R} \right)^{3\kappa} - \frac{2\sigma}{R} - \frac{4\mu}{R} \left(\frac{dR}{dt} \right) - P_0 + P_v + p \right] \quad (1)$$

where R is the radius of cavitation bubble, R_0 is the initial radius of bubble, P_0 is the initial pressure, P_v is the vapor pressure, p is the external acoustic pressure, σ is the surface tension, μ is the fluid viscosity, and κ is the polytropic exponent. This simulation does not consider the variation of the ultrasonic intensity and the liquid temperature. The gas and vapor are incompressible. The motion of cavitation bubble wall is set as spherical symmetric movement.

To calculate the cavitation behavior under single-frequency ultrasonic vibration, the p in Eq. (1) is defined as $p = P_m \sin(2\pi f t)$, where P_m is the acoustic pressure amplitude and f is the frequency of ultrasound. **Table 1** lists the parameters used in this calculation.

Figure 1 shows the effect of ultrasonic frequency on cavitation bubble's behavior in magnesium alloy. It notes that frequency has strong effect on bubble's behavior. Ultrasound with lower frequency generally has larger-sized cavitation bubbles. The 22 kHz is an important frequency, which can be defined as the threshold frequency of instantaneous cavitation for magnesium alloy. When the frequency is larger than 22 kHz, bubbles usually suffer several shrinkages and expansions before collapse. It also notes that ultrasound with higher frequency is not beneficial to the melt treatment of magnesium alloy. The initial radius of bubble is another key to cavitation. **Figure 2** shows the effect of bubble's radius on cavitation behavior of magnesium alloy. Small initial bubble changes regularly under single-frequency ultrasonic vibration. When bubble's radius is close to resonance frequency, cavitation bubble's radius changes rapidly in a short time. It should be pointed out that the initial bubble in magnesium melt is provided by hydrogen bubble, suggesting that they cannot be controlled.

Name	Value	Description
R_0	0.1–100 μm	Initial radius of cavitation bubble
P_0	$1.013 \cdot 10^5$ Pa	Initial pressure outside cavitation bubble
P_v	1000 Pa	Vapor pressure within cavitation bubble
σ	0.564	Surface tension
μ	$1.12 \cdot 10^{-3}$	Fluid viscosity
κ	1.34	Polytropic exponent
f	20 KHz	Initial frequency of another wave
P_m	$1.01 \cdot 10^6$ Pa	Acoustic pressure amplitude

Table 1.
Parameters and initial values for Eq. (1).

When dual-frequency ultrasonic field (DUF) is introduced to magnesium melt, the cavitation behavior becomes completely different, as shown in **Figure 3**. Small bubble's radius becomes irregular. It is worth to note that bubble becomes larger under dual-frequency ultrasonic field. The bubble cannot collapse within 250 μs when the initial radius is over 15 μm under single-frequency ultrasonic field, but

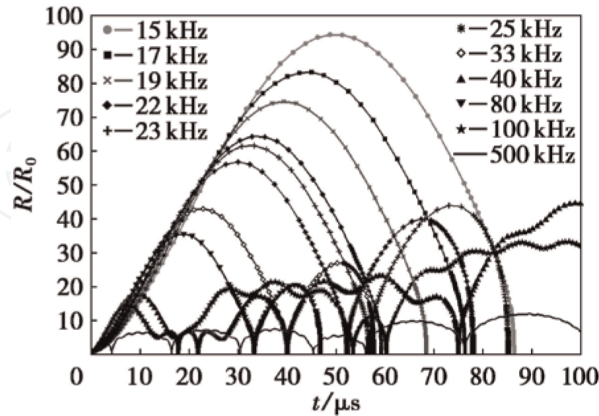


Figure 1.
 Cavitation bubbling behavior with different ultrasonic frequencies.

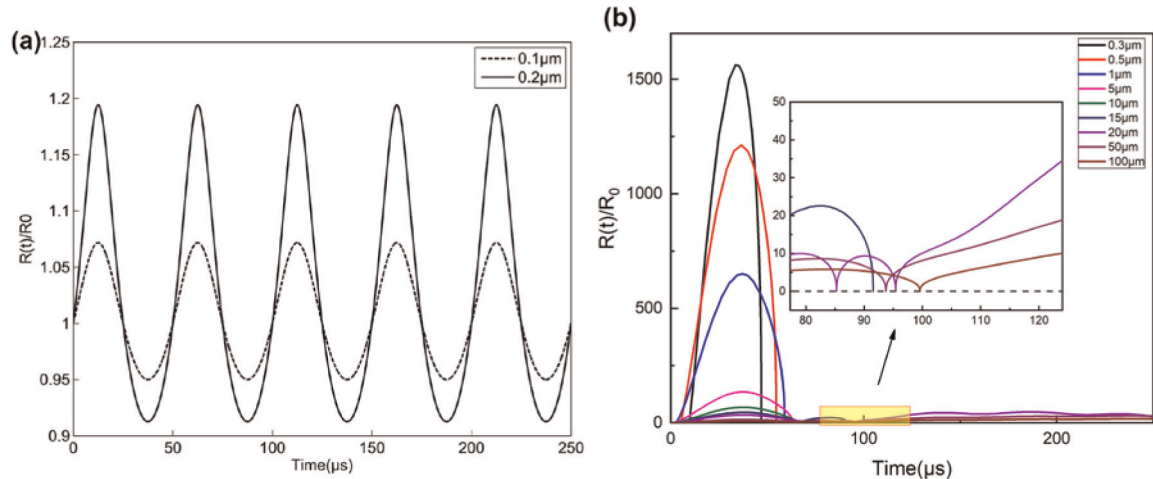


Figure 2.
 Cavitation bubbling behavior with different initial bubble radii under single-frequency ultrasonic field: (a) 0.1 μm and 0.2 μm ; (b) 0.3-100 μm .

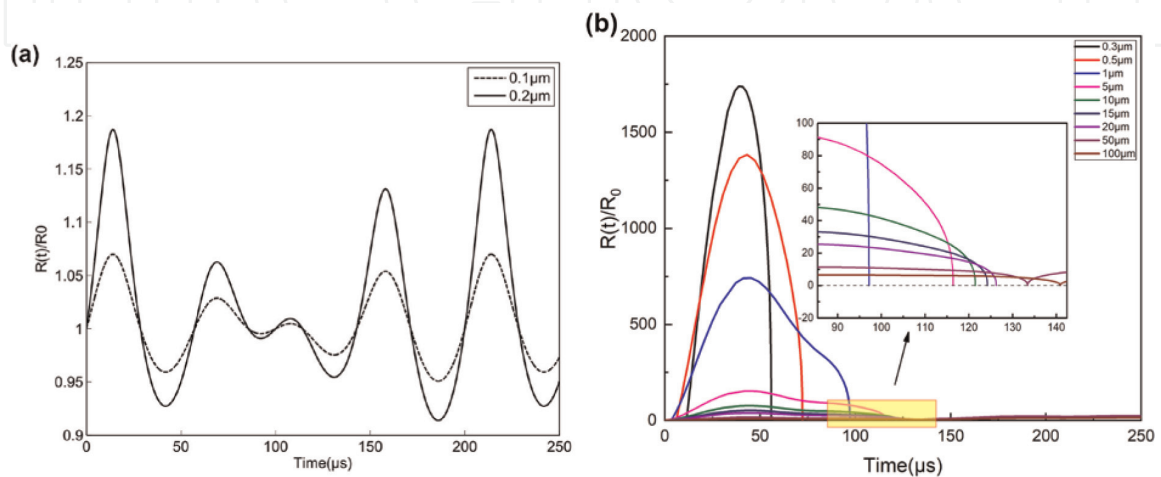


Figure 3.
 Cavitation bubbling behavior with different initial bubble radii under dual-frequency ultrasonic field: (a) 0.1 μm and 0.2 μm ; (b) 0.3-100 μm .

this limitation is expanded to 20 μm under dual-frequency ultrasonic field. Thus, the dual-frequency ultrasonic field has great potential to enhance the cavitation in magnesium alloy, and the experimental results are shown in Section 6 of this chapter.

3. Effect of ultrasonic treatment on melt structure

The ultrasonic vibration is a mechanical wave. When the wave propagates in the magnesium melt, molecules suffer regular vibration, which can change the melt structure. To investigate this issue, we employ the electrical resistivity to character the melt structure. The experimental setup is shown in **Figure 4**. The four-electrode method is used. The tested melt is Pb–Sn liquid metal. The electrical resistivity ρ is calculated by

$$\rho = [R - (R_e + R_w + R_c)]S/L \quad (2)$$

where R is the total electrical resistance, R_e is the resistance of electrodes, R_w is the resistance of wire, R_c is the contact resistance, S is the cross area of melt, and L is the length of melt. In order to avoid the interference of ultrasonic horn during measurement, the horn is coated by $\text{ZrO}_2\text{-CaO}$.

Figure 5 displays the variation of electrical resistivity for the Pb–80 wt.%Sn melt at 553 K and the relevant microstructure evolution. Four stages for the electrical resistivity ρ are observed. The resistance keeps stable at ρ_0 before ultrasonic vibration. The resistance reduces to ρ' immediately when the ultrasound is introduced to the melt. The drop is defined as $\Delta\rho$. The resistance rises to ρ'' instantaneously once the ultrasound disappeared. In addition, the $\Delta\rho'$ is defined to describe the difference between ρ_0 and ρ' . It is also found that the ρ stays at ρ'' for Δt_1 ($\Delta\rho' = \rho_0 - \rho''$). After the holding time Δt_2 , the ρ returns to the initial value (ρ_0). The microstructure evolution is shown in **Figure 5** as well. Without ultrasonic treatment, developed dendrites and large columnar crystals are observed with some branch length of $\sim 400 \mu\text{m}$, as shown in **Figure 5(a)**. Microstructure is dramatically refined with ultrasonic vibration 5 min after treatment. With the increase of holding time, the microstructure also recovers to the initial status gradually.

In this work, the modified band theory is employed to understand the electrical properties of melt. Thus, the dimensionless parameter δ is introduced to show the disorder degree of electrons:

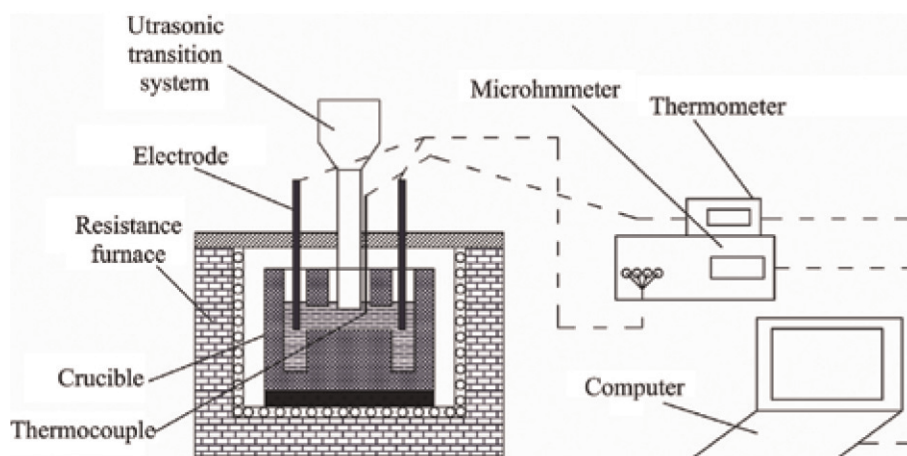


Figure 4.
Schematic of the experimental setup for electrical resistivity tests.

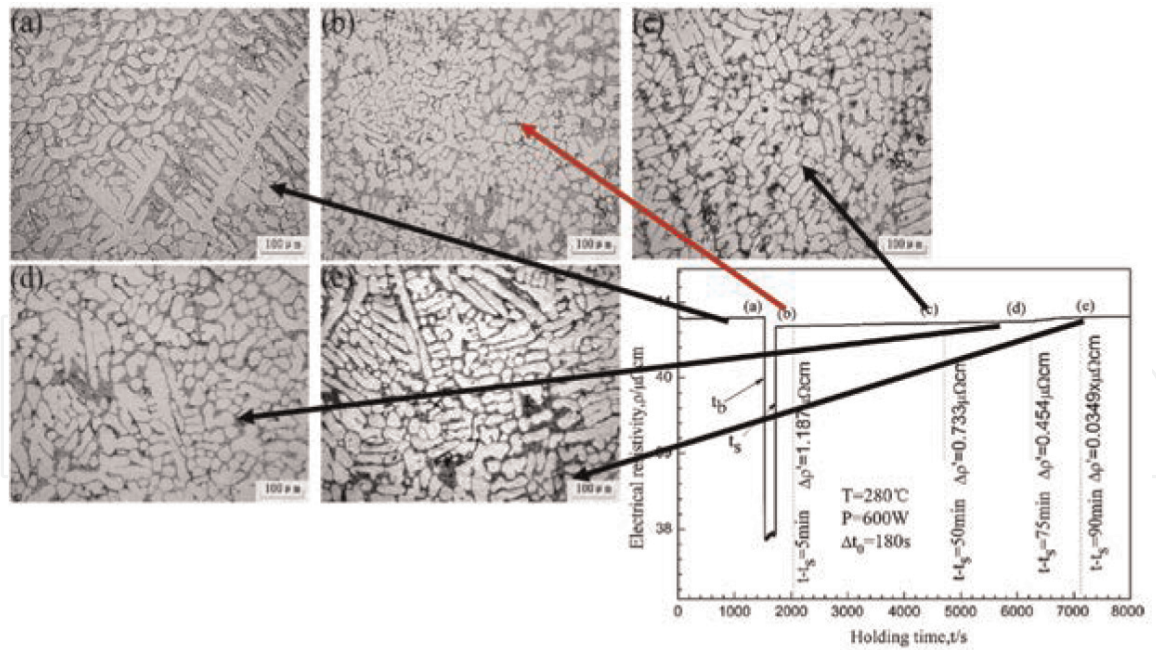


Figure 5. Electrical resistivity ρ vs. the holding time t for the Pb–80 wt.%Sn melt at 553 K and microstructure evolution.

$$\delta = W/B \quad (3)$$

where W and B represent the width of electron energy' distribution and energy band, respectively. There is a strong relativity between the degrees of system disorder and localization of electron [6]. The number of localized electrons increases with the rise of disorder degree of the system. In addition, the localized electrons are adverse to the electrical conductivity, while the extended electrons are beneficial to the conductivity. Therefore, the electrical conductivity (σ) associated with the energy band theory is shown as follows:

$$\sigma = ne^2\tau(E_F)/m^* \quad (4)$$

where n represents the number density of extended electrons in the investigated liquid, τ represents the electron's free time, m^* represents the effective mass, and E_F is the Fermi energy. Thus, the number density of extended electrons holds the key to the electrical conductivity of melt, based on Eq. (4).

When ultrasound is introduced into the Pb–Sn melt, the atoms are forced to vibrate due to the characteristics of sound wave. Then the disordered atoms become “well-organized” under ultrasonic field, which means that the disorder degree of the melt is reduced. Thus, with the decrease of disorder degree, the W is reduced, and consequently, the number density of extended electrons is increased, resulting in the improvement of electrical conductivity.

The forced vibration disappears when the ultrasonic vibration is stopped. “Well-organized” atoms recover their disorder degree, increasing the number density of localized electron. It is worth to notice that a long time is required to recover the initial value of resistivity, suggesting that the ultrasonic treatment can change the short-ordered structures (SROs) of melt [7].

4. Ultrasonic degassing of magnesium alloy

Degassing is always a significant process during the melting of magnesium alloys [8–10]. At the end of solidification process, micropores are formed because of the

pressure decrease of interdendritic flow or existence of dissolved gaseous elements in the liquid alloy. To degas and purify the melt, researchers have developed some technologies such as gaseous chlorine, hexachlorethane (C_2Cl_6), rotating impeller degasser with argon, and ultrasonic degassing. Among these methods, the ultrasonic degassing is the most convenient way without polluting the melt. The flux and argon are employed to help ultrasonic degassing reach the best efficiency. **Figure 6** shows the experimental equipment. A channel is set inside the ultrasonic horn as the path for argon and flux powders.

Figure 7 shows the hydrogen content with the increase of holding time by different degassing technologies. The initial value of hydrogen content is 22.5 ppm, which reduces dramatically after degassing process. It notes that the ultrasonic argon degassing technology has the highest efficiency, displaying the lowest level of hydrogen content in the same time. It is interesting to note that the degassing efficiency of ultrasonic degassing technology is lower than the argon degassing technology. The hollow ultrasonic horn should be responsible for this drop, which reduce the propagation efficiency of ultrasound.

For magnesium alloy, the hydrogen is removed by the tiny and dispersed argon gas bubbles. The hydrogen starts accumulating in argon gas due to the balance with

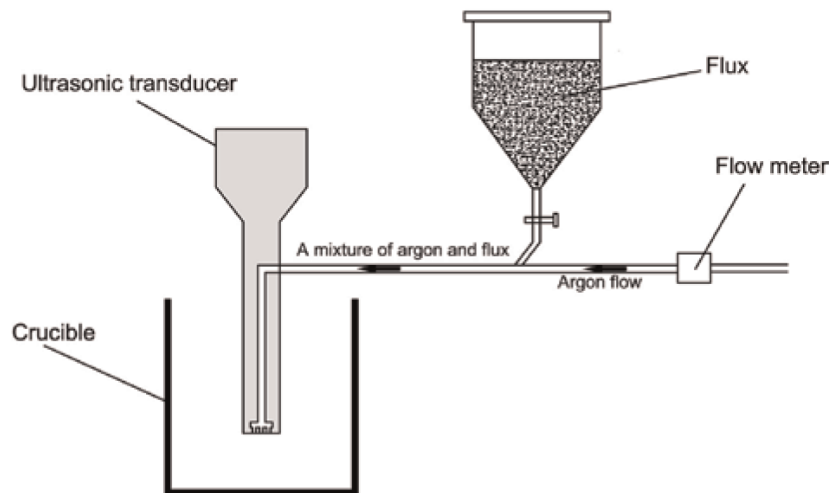


Figure 6.
The schematic of the experimental equipment for ultrasonic degassing.

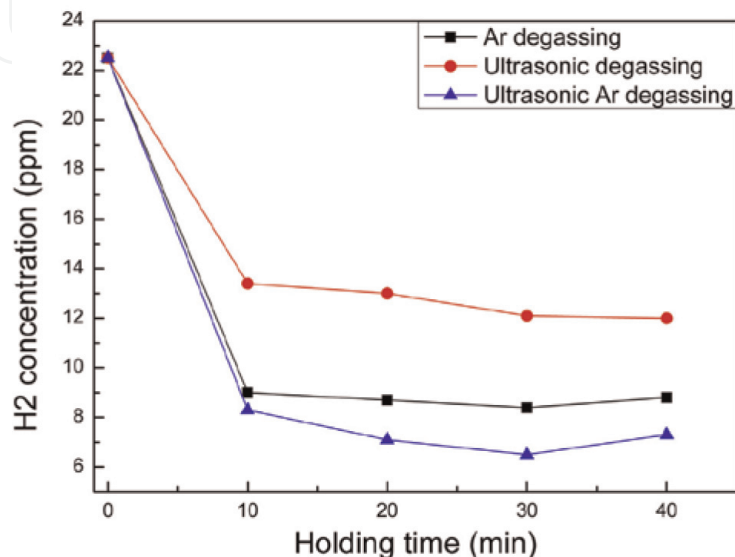


Figure 7.
Hydrogen content as a function of holding time in different degassing processes.

the dissolved concentration in the melt. The hydrogen transports from the melt to the bubble boundary firstly. The hydrogen reacts and become the hydrogen gas. Finally, the hydrogen is transported away as the gas forms.

According to the results above, the hydrogen concentration has functional relation with time of purification t [11]:

$$[H]/[H]_0 = \exp[-(k\rho S/M) \cdot t] \quad (5)$$

where k is the mass transfer coefficient; ρ is the density of magnesium melt; S is the bubble's surface area; $[H]_0$ is the initial hydrogen content; and M is the weight of magnesium melt.

Obviously, the hydrogen content decreases with the increase of degassing time while the point is improving the degassing efficiency. Based on Eq. (5), the degassing efficiency is determined by the mass transfer coefficient k and the total surface area of the bubbles S in the same time. Thus, to promote the degassing efficiency, increasing the k and S is feasible. The bubble's surface area is driven by

$$S = 3\dot{G}h/vr = 3\dot{G}\tau/r \quad (6)$$

where h is the bath height; v is the velocity of bubble; r is the radius of bubble; and τ is the residual time in the melt. The velocity of bubble has a strongly positive relation with its radius [12], suggesting that larger bubble usually has higher velocity. However, the mass transfer coefficient k has negative relation with the bubble's diameter, implying small bubble has higher k value. Thus, to raise the degassing efficiency, employing the small sized bubble is critical.

The cavitation and rectified mass diffusion are two mechanisms for ultrasonic degassing process. Cavitation bubble is formed when the acoustic pressure surpasses the cavitation threshold. Generally, there are two nucleating mechanisms for cavitation, namely, the microscopy gas cavities and non-wettable particles. In case of magnesium melt, both of two mechanisms are applicable, due to the large content of oxides and high level of hydrogen solubility. The cavitation bubble starts expanding and shrinking under the alternating pressure. The dissolved hydrogen can diffuse into the cavitation bubble during the shrinkage process, so-called rectified mass diffusion. In this way, hydrogen is accumulated to form large gas bubble which can escape from the melt.

It is noticed that the argon-ultrasonic degassing has best efficiency. Interaction between argon and ultrasound should respond to this result. Firstly, the argon gas is purified through the center of ultrasonic horn. The purified argon bubbles start expanding and shrinking because of the propagation of ultrasound. These bubbles can be broken into dense small bubbles under high-intensity acoustic pressure, increasing the surface area of bubble. Besides, the rectified mass diffusion effect brought by ultrasonic vibration can encourage hydrogen diffusing to the argon bubbles. In addition, the acoustic streaming can carry the refined argon bubble to the whole melt. What is more, the argon bubbles can also improve the forming of cavitation and make bubbles easily to ascend to the melt surface. Therefore, these mechanisms work together and promote the degassing efficiency.

5. Effect of ultrasonic melt treatment on microstructure of magnesium alloy

Magnesium alloys have a unique structure, namely, the HCP structure, which has limited slip system. In addition, magnesium alloy has a large Hall-Petch slope, k , according to the relationship $\sigma = \sigma_0 + kd^{-1/2}$. These two characteristics make the

grain refinement become one of the important methods to improve the mechanical properties and the workability of magnesium alloy. Ultrasonic melt treatment has proved its ability to control and refine the solidification structure for many alloys. We investigated the ultrasonic treatment on microstructure evolution of magnesium alloys [13, 14].

The experimental setup for this study is shown in **Figure 8**. The treatment system includes a resistance furnace, an iron crucible, a water tank, and an ultrasonic vibration system with the maximum power of 2000 W. The ultrasonic vibration system is composed by an ultrasonic generator, a magnetostrictive transducer, and a mild steel-made acoustic horn.

One of the widely used commercial magnesium alloys, AZ80 alloy, was chosen in this work. Its chemical composition (wt.%) was as follows: Al 8.0, Zn 0.6, Mn 0.15, and Mg balance. The prepared materials were melted in the crucible with heating by the resistance furnace and protection of CO₂ + 0.5% SF₆ atmosphere. The temperature of melt maintained at 650°C for 600 s. The preheated ultrasonic horn (650°C) was inserted 0.02 m under the surface of melt. After treatment, the melt was quenched in the water tank immediately.

The microstructures of as-cast AZ80 alloy without and with ultrasonic treatment are shown in **Figure 9(a)** and **(b)**, respectively. Coarse dendrites and large-sized

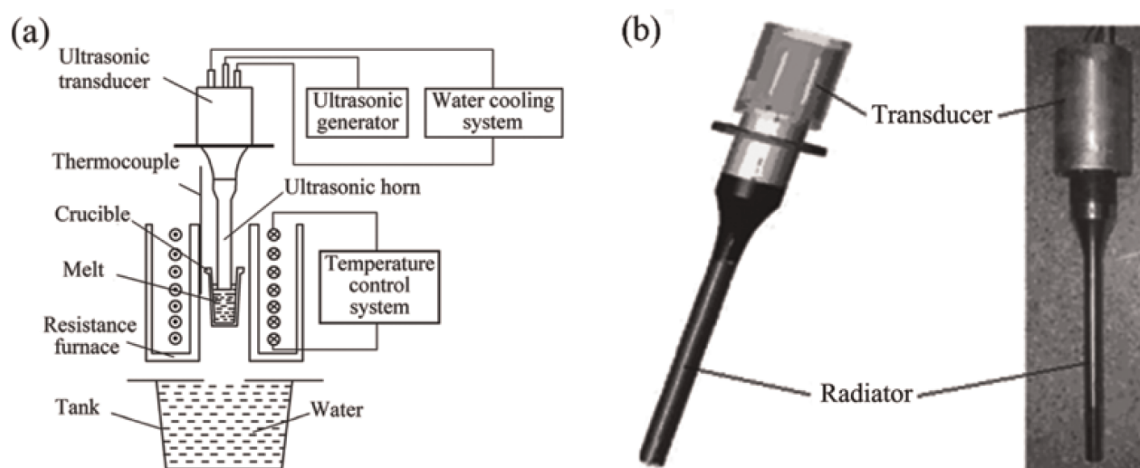


Figure 8. (a) Schematic image of experimental apparatus and (b) structures of ultrasonic transducer and ultrasonic radiator.

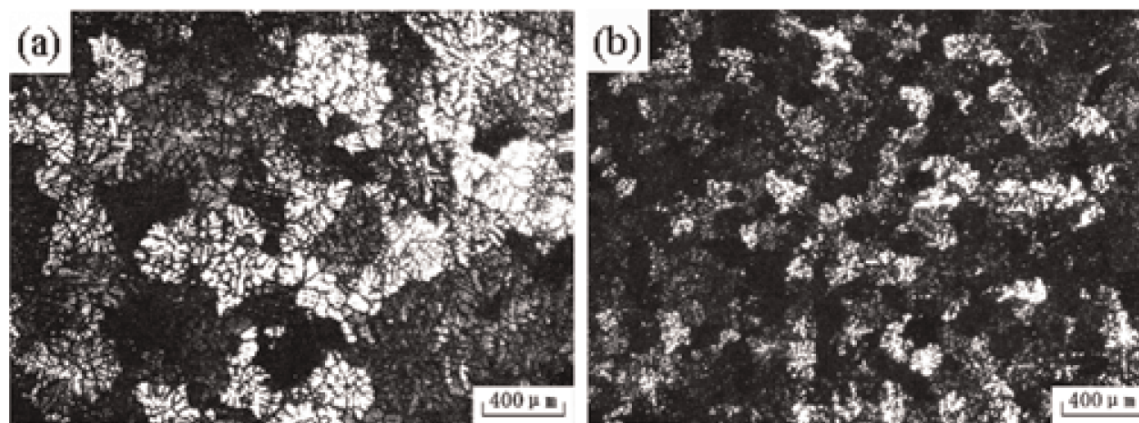


Figure 9. Microstructure of the AZ80 alloy casted (a) without ultrasonic and (b) with 600 W ultrasonic treatment ($\varphi 0.02$ m ultrasonic emitter used).

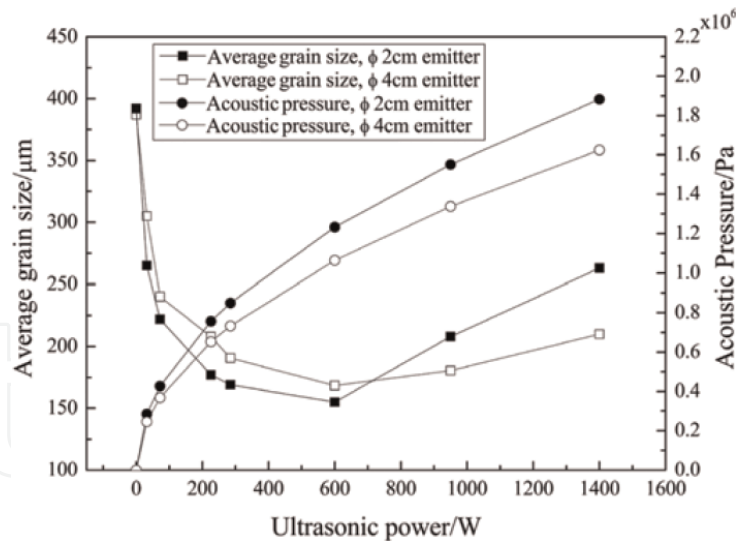


Figure 10. Influence of ultrasonic power on the grain size of the AZ80 ingot and the relevant acoustic pressure associated with treated sample (solid mark, $\phi 0.02$ m ultrasonic emitter used; hollow mark, $\phi 0.04$ m ultrasonic emitter used).

primary grains are observed with the grain size of about $387 \mu\text{m}$, suggesting the typical dendrite growth mode. With ultrasonic treatment, the grain size is rapidly reduced to $147 \mu\text{m}$ with the observation of globular and even primary grains. In addition, the homogeneity is improved as well. **Figure 10** shows the effect of ultrasonic power on grain refinement efficiency of AZ80 alloy in the same treatment time and the relation between acoustic pressure and ultrasonic power. When the ultrasonic power rises from 0 to 600 W, the acoustic pressure increases, but the grain size shows adverse trend, suggesting better grain refinement efficiency. With the further increment of ultrasonic power, the acoustic pressure continues to rise, while grain size stops reducing. In this case, the best grain refinement efficiency appears at 600 W.

The grain refinement of AZ80 magnesium alloy of the ultrasonic treatment can be attributed to the ultrasonic cavitation. The ultrasonic cavitation can bring two influences which can affect the nucleation and growth of grains, so-called cavitation-enhanced nucleation and cavitation-induced (shock waves) dendrite fragmentation [15, 16]. In this work, the treatment temperature is 40°C higher than the liquidus temperature of treated alloy, which means that the cavitation-induced dendrite fragmentation does not work and has no contribution on the grain refinement. Therefore, the cavitation-enhanced nucleation is the main reason that caused the grain refinement. The ultrasonic cavitation can clean the surfaces of the poorly wetted particles in the melt, and consequently, these particles become the nucleation points, increasing the number of primary magnesium grains. With the help of acoustic streaming, these effective nucleation sites are carried to the whole melt. Note the ultrasonic cavitation works when ultrasonic pressure exceeds the cavitation threshold. Thus, strong acoustic pressure can enlarge and enhance the cavitation effect. With the increase of ultrasonic power, the acoustic pressure is increased, which brings better efficiency of grain refinement. However, the results reflect that higher ultrasonic power, e.g., 950 W or even 1400 W, cannot further enhance the grain refinement efficiency but weaken it. When the cavitation bubble collapses, high temperature and pressure are released in melt, so-called thermal effect. The higher ultrasonic power may also increase the thermal effect. Therefore, the cooling rate is reduced, which is beneficial to the growth of grain but has adverse effect on grain refinement caused by ultrasonic treatment.

6. Dual-frequency ultrasonic treatment on solidification behavior of magnesium alloy

In Section 1, we discussed about the effect of dual-frequency ultrasound on cavitation bubble's behavior in magnesium melt. In this section, we will show the experimental results. In recent decades, dual-frequency acoustic vibration has been employed in sonochemistry, medical diagnostics, and fluid engineering. For example, the dual-frequency ultrasonic wave can enhance the extraction rates of leaching process and improve the enzymolysis of corn gluten meal [17]. The dual-frequency ultrasonic vibration mode is also used to detect the fluid pressure and the bubble density in liquid [18, 19]. Also, dual-frequency ultrasound can help increase the accuracy of biomedical diagnosis. We firstly employed the dual-frequency ultrasonic field (DUF) to treat the magnesium alloy and investigated its solidification behavior [20].

Figure 11 shows the experimental apparatus used in this work. Two self-governed ultrasonic systems were used simultaneously. The frequency of two systems is 15 and 20 kHz, respectively. Each ultrasonic vibration system is made up by an ultrasonic power supply, an ultrasonic transducer, an acoustical waveguide, and a Ti6Al4V acoustic horn. A vortex tube cooler was used to ensure the comfortable working environment of transducer. The commercial ZK60 was chosen as the treated magnesium alloy.

Figure 12(a)–(f) displays the optical images of as-cast ZK60 alloys with and without different ultrasonic treatments. Without ultrasonic treatment, developed dendrites and coarse grains are observed with large size. Similar with the results in Section 5, the SUF can refine the α -Mg grains in some degree with the disappearance of dendrites. The DUF can considerably refine the α -Mg grains, and the refinement efficiency is different according to electric power. The morphology of α -Mg grains also changes a lot, showing the fine and globular form. The grain size of

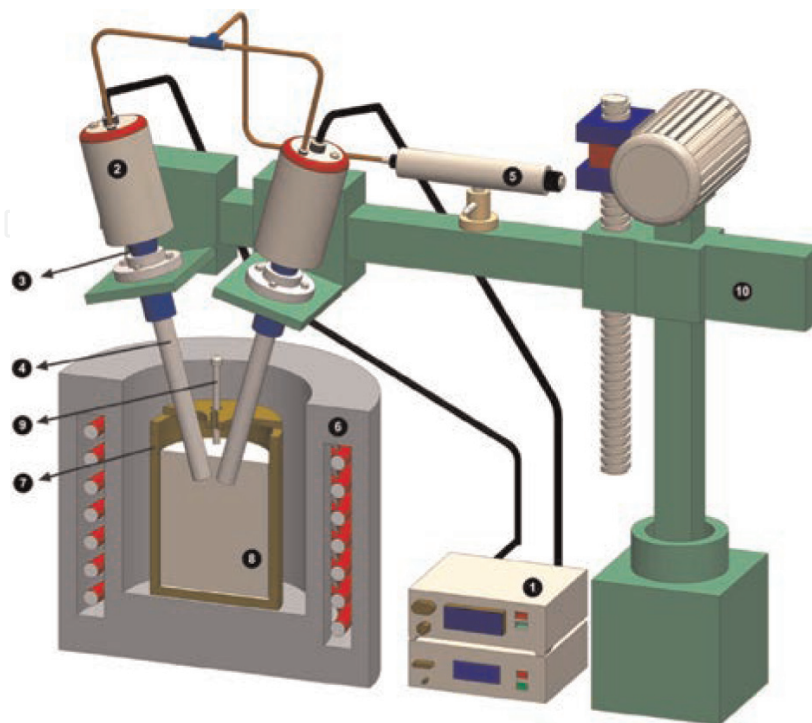


Figure 11. Schematic image of the experimental apparatus: (1) ultrasonic power supply, (2) ultrasonic transducer, (3) acoustical waveguide, (4) acoustic radiator/horn, (5) vortex tube cooler, (6) resistance furnace, (7) iron crucible, (8) magnesium melt, (9) thermocouple, (10) positioning device.

untreated and SUF-treated ZK60 alloys is $183 \pm 8 \mu\text{m}$ and $125 \pm 6 \mu\text{m}$, respectively. In the same total electric power, the DUF makes the grain size reduce to $72 \pm 6 \mu\text{m}$. Increasing the electric power, the grain size reduces to $59 \pm 4 \mu\text{m}$ (1000 W) and $50 \pm 3 \mu\text{m}$ (1400 W), while further increment of electric power cannot decrease the grain size but rise to $58 \pm 3 \mu\text{m}$ after 1800 W DUF treatment, which has the same results in Section 5.

Now it is clear that the DUF has the higher refinement efficiency than SUF in the same total electric power. To better explain the mechanism of ultrasonic treatment on grain refinement of the investigated alloy, a schematic image is given based on the microstructure observation, as shown in **Figure 13**. The ZK60 melt suffered cyclic alternating acoustic field, when the ultrasonic vibration is introduced. The liquid molecules are pulled to form the cavitation bubbles in negative acoustic period. The enlargement and formation of cavitation bubble can absorb heat from the melt, resulting in the local supercooling on the surface of bubbles, as shown in **Figure 13(a)**. Consequently, nucleation can easily occur on bubble's surface,

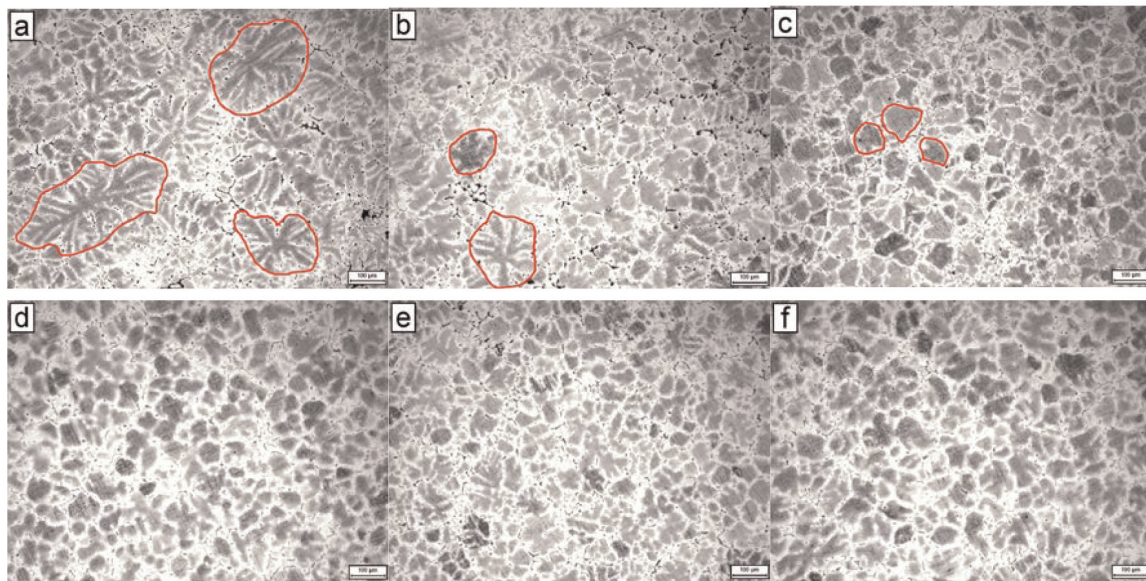


Figure 12.
 Optical images of as-cast ZK60 alloys with different ultrasonic treatments: (a) without ultrasonic treatment; (b) SUF treatment with 1200 W; and DUF treatment with (c) 600 W; (d) 1000 W; (e) 1400 W; and (f) 1800 W electric power.

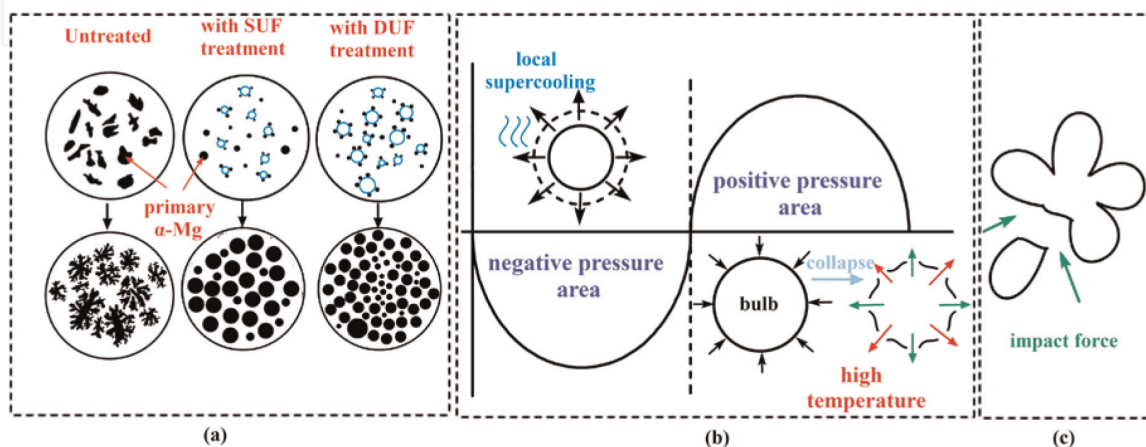


Figure 13.
 Schematic image of mechanisms of ultrasonic grain refinement: (a) cavitation-enhanced heterogeneous nucleation; (b) formation, growth, and collapse of the cavitation bubble; and (c) dendrite fragmentation caused by impact force.

increasing the number of primary nuclei. In the positive acoustic pressure period, the cavitation bubble collapsed, releasing the high temperature and strong impact force (seen in **Figure 13(b)**). This impact force fragments dendrites and primary Mg nuclei (as shown in **Figure 13(c)**), by which the number of nuclei is also raised. Finally, the acoustic streaming, a liquid flow due to acoustic pressure gradient, transports the increased nuclei through the whole magnesium alloy melt.

In Section 1, the numerical results show that the DUF can produce larger cavitation bubbles and increase the number of instantaneous bubbles. Thus, these two improvements enhance the grain refinement efficiency. Larger cavitation bubble can absorb more heat from melt during its growth process, by which the heterogeneous nucleation caused by ultrasonic treatment is improved (as shown in **Figure 13(a)**). In addition, stronger impact force is released by larger cavitation bubble, which enhances the fragmentation of primary grains.

Besides α -Mg grain, the ultrasonic treatment also has ability to change the morphology of β -phase in ZK60, as shown in **Figure 14**. A large number of lamellar β -phases are observed in untreated sample. There are few dot-like β -phase in the α -Mg matrix. The SUF makes some lamellar β -phase become the strip-like form. The number of dot-like β -phase increases. A lot of tiny dot-like β -phases with dispersed distribution can be observed after DUF treatment. The energy-dispersive spectroscopy (EDS) results reflect these three aerial Mg-Zn phases.

To further confirm the type of these phases, XRD tests are carried out, as shown in **Figure 15**. Thus, in combination with the XRD patterns and EDS results (**Table 2**), three β -phases observed from SEM images are laves phases (MgZn_2). It also notes that the ultrasonic treatment cannot change the phase constitutions magnesium alloy, while it is interesting to find that the orientation of α -Mg is changed. According to partial enlarged drawing of **Figure 15**, the ultrasonic treatment reduces the intensities of diffraction peaks corresponding to (021) and (004) crystal surface of α -Mg but increases the diffraction peak intensity of (112) crystal surface.

Such changes associated with the evolution of β -phase are ascribed to the acoustic streaming. During the solidification process, the Zn element is enriched on the grain boundaries usually, which makes the laminar MgZn_2 phase to form easily. When ultrasonic vibration is introduced in the melt, acoustic streaming accelerates

Positions	Element (at%)		
	Mg	Zn	Total
A	61.11	38.89	100
B	70.96	29.04	100
C	65.36	34.64	100

Table 2.
EDS results of positions in **Figure 14**.

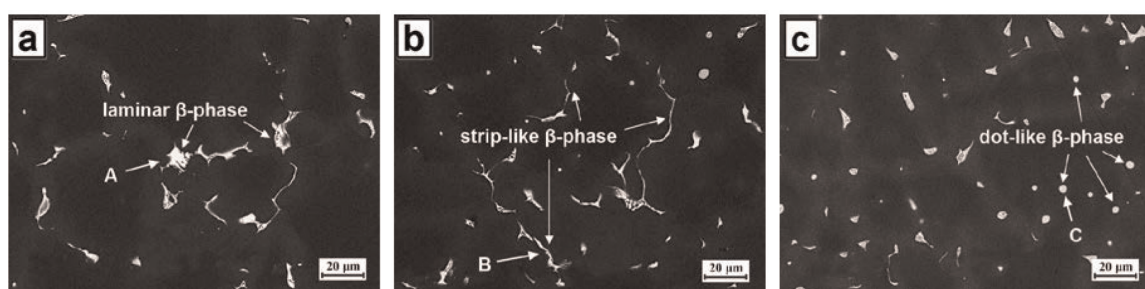


Figure 14.
SEM images of the β -phase in as-cast ZK60 alloys (a) without ultrasonic treatment; (b) with 1200 W SUF treatment; and (c) with 600 W DUF treatment.

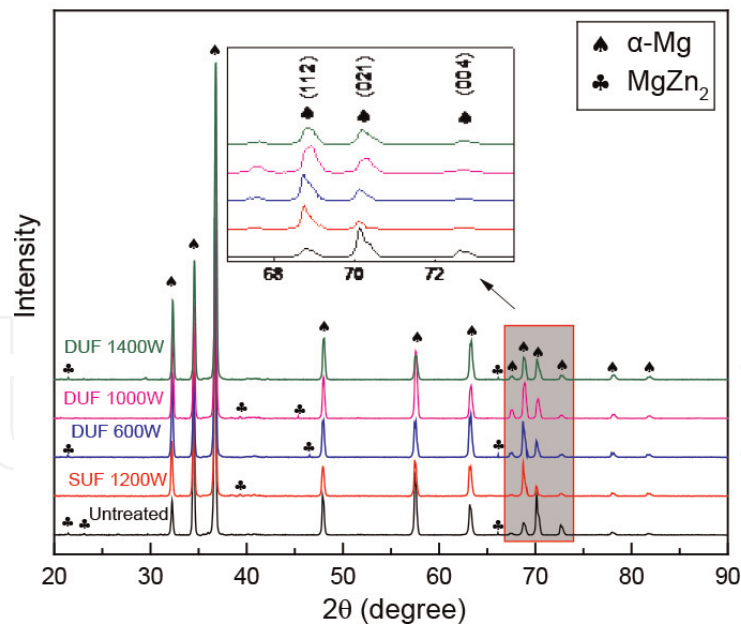


Figure 15.
XRD patterns of as-cast ZK60 alloys treated by different ultrasonic conditions.

the heat and mass transfer and then relieves the enrichment of Zn element. Thus, tiny and dot-like $MgZn_2$ phases are produced with dispersed distribution.

7. Ultrasonic melt treatment on DC casting process of magnesium billet

In the above sections, the ultrasonic treatment is employed to treat the magnesium melt in laboratory scale with small volume of melt. This section displays the application of ultrasonic treatment in direct-chill (DC) casting of magnesium billet. The DC casting method is the most popular way to produce large-sized magnesium billet [21]. However, due to the unique features of magnesium alloys, coarse grains, developed dendrites, wide columnar crystal area, and inhomogeneous structure appear in billet usually, which have adverse effect in subsequent processing. The traditional ultrasonic treatment technology generally has limited action area and then cannot satisfy the requirement of the treatment for large volume melt. Therefore, to overcome this weakness, we apply a unique ultrasonic treatment technology, namely, the variable-frequency ultrasonic treatment technology. In addition, the electromagnetic field is also a helpful external field for DC casting of magnesium alloys. In this section, we will show you the comparison of traditional fixed-frequency field (SUF), variable-frequency ultrasonic field (VUF), and low-frequency electromagnetic field (LEF) on DC casting of magnesium alloy. The interaction between LEF and VUF is also discussed [22–24].

Figure 16 demonstrates the experimental apparatus for ultrasonic DC casting. Three synergistic systems constitute the whole experimental setup, namely, the casting system, the low-frequency electromagnetic system, and the ultrasonic vibration system. The ultrasonic wave was provided by a self-designed ultrasonic vibration system, which comprised an ultrasonic generator, an ultrasonic transducer, a waveguide, and a 35 mm diameter stainless steel acoustic horn. The ultrasonic generator could produce two kinds of ultrasonic vibration fields, namely, the fixed-frequency ultrasonic field (FUF) and variable-frequency ultrasonic field (VUF). The frequency of FUF was fixed at 20 kHz, while the VUF had a 20 kHz center frequency and a 200 Hz changing frequency. The electromagnetic control unit and the induction coil provided the low-frequency electromagnetic field (LEF). The frequency of LEF was 20 Hz and the alternating current was 150 A. A resistance

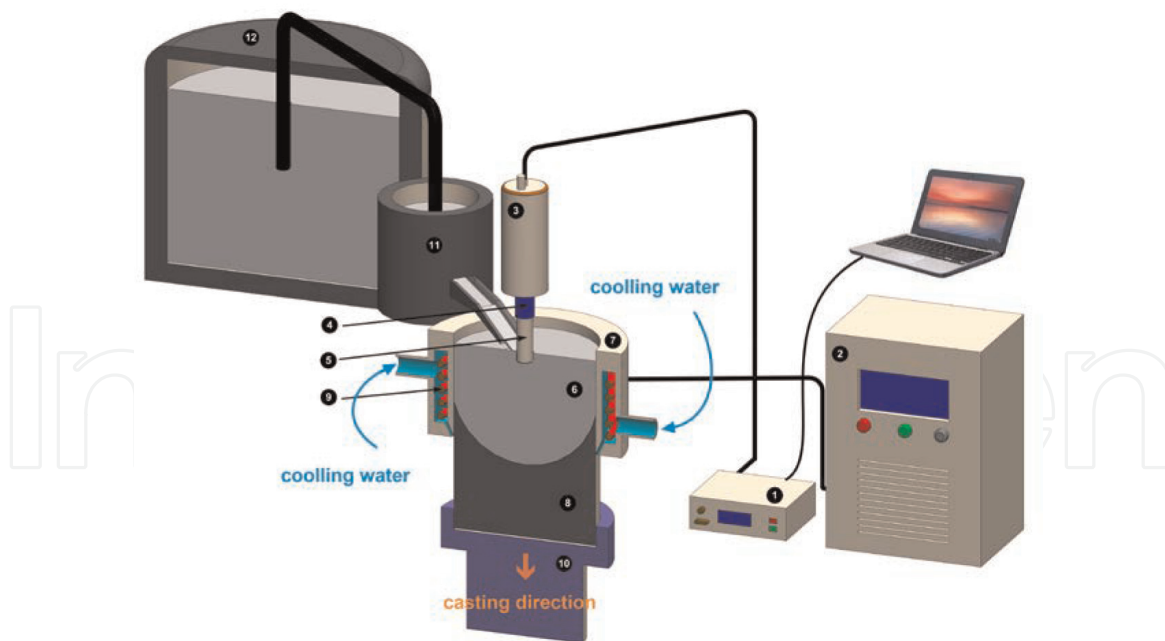


Figure 16.

Schematic image of the experimental apparatus: (1) ultrasonic power supply, (2) electromagnetic field control unit, (3) ultrasonic transducer, (4) acoustic waveguide, (5) acoustic radiator/horn, (6) magnesium alloy melt, (7) crystallizer, (8) billet, (9) magnetic coil, (10) dummy bar, (11) tundish, and (12) smelting furnace.

furnace, a crystallizer with the Ø255 mm aluminum ring, a tundish, and a casting control unit compose the casting system.

At first, the commercial pure magnesium, pure aluminum, pure zinc, and anhydrous MnCl_2 were melted in a resistance furnace at 740°C with the protection of $\text{CO}_2 + 0.5\% \text{SF}_6$ (1:2) atmosphere. As shown in **Figure 16**, the melt was transferred to the crystallizer at the temperature of 670°C from the crucible. With the downward movement of the casting machine, the AZ80 billets (Ø255 mm) were made. During the casting process, the preheated ultrasonic horn was inserted 50 mm under the interface of the melting liquid in order to introduce the ultrasonic vibration into the melt. In the same time, the LEF worked together to input the electromagnetic field. Samples for microstructure characterization were ground by the different grades of SiC papers and then polished and etched using a solution of 4.2 g picric acid to reveal their microstructures. The characterizations of microstructure were obtained using an optical microscopy (OM) and a scanning electron microscopy (SEM) with energy-dispersive spectroscopy (EDS).

Figure 17 displays the microstructure of as-cast AZ80 billet casted with different external field treatments. Obviously, a wide columnar crystal zone is observed in the center of billet with approximate 22.2 mm length. The α -Mg grains are coarse with large grain size and high degree of inhomogeneity. The FUF treatment refines the grains located in the center area but has little effect on the edge of billet. The grain refinement efficiency decreases from center to edge of billet. It is interesting to find that the columnar crystal area disappears. The LEF also has ability to refine α -Mg grains, while its refinement tendency is different from the FUF, showing increase trend from center to edge of billet. The LEF can only reduce the width of columnar crystal area to columnar crystal area to 12.8 mm. The VUF treatment shows the best grain refinement capacity. All the grains along center to edge become very small with global form. In addition, grains have homogeneous distribution in whole billet. With VUF and LEF treatment, the grain is also refined dramatically with the enhancement of homogeneity as well. It notes that the LEF + VUF may further promote the refinement efficiency.

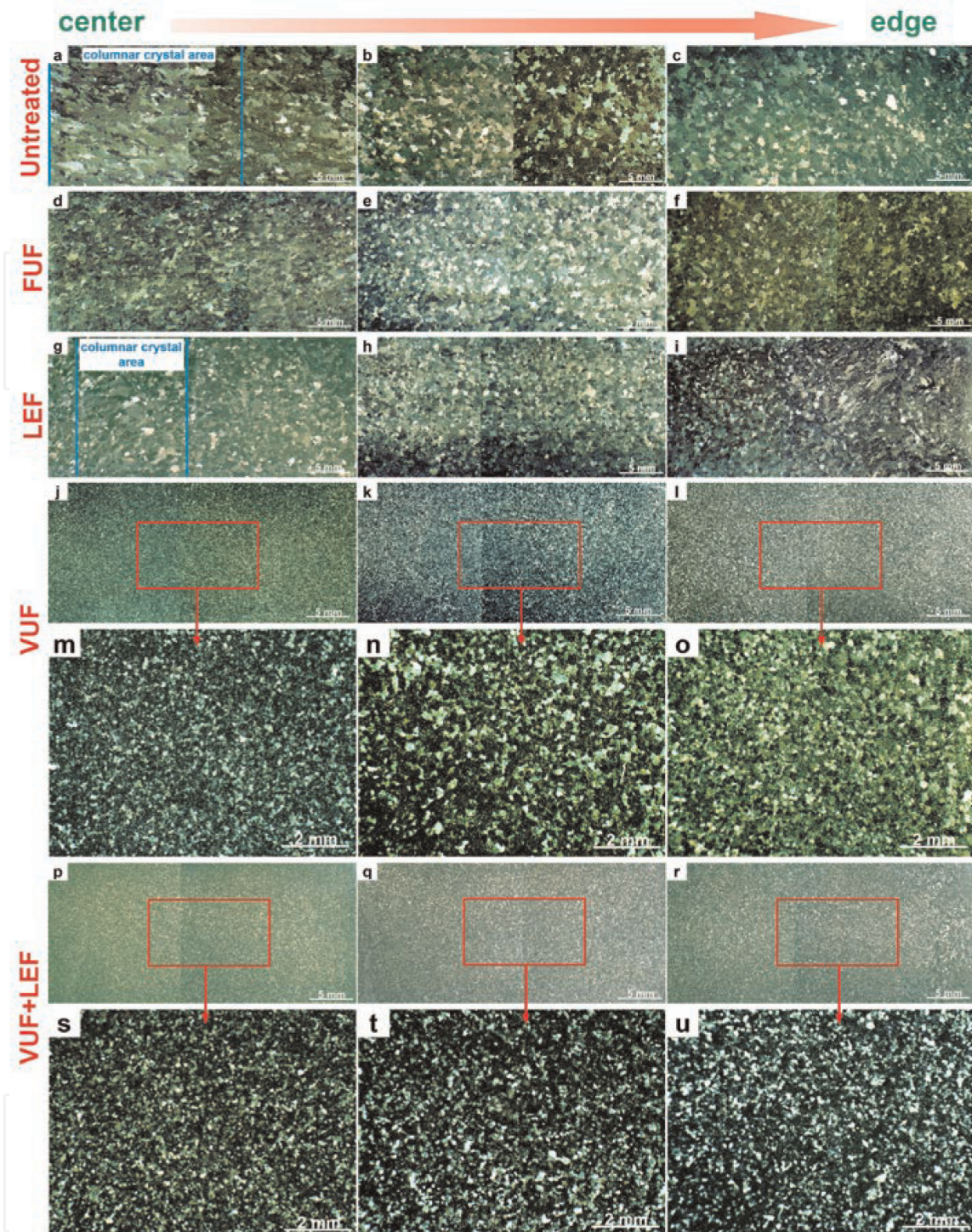


Figure 17. Microstructure from center to edge of as-cast AZ80 billet with different external field treatments: (a)–(c) without external field; (d)–(f) with FUF treatment; (g)–(i) with LEF treatment; (j)–(l) with VUF treatment; (p)–(r) with VUF + LEF treatment; (m)–(o) and (s)–(u) are partial enlarged picture.

Figure 18 reflects the statistic of grain size and its distribution of as-cast AZ80 treated by different external fields. The grain size of untreated billet is 679–1454 μm which reduces to 752–916 μm with FUF treatment. The value associated with the LEF treatment is lower than FUF showing a figure of 732–1027 μm . The VUF displays the excellent refinement efficiency, with the grain size of 150–241 μm . This value is further reduced to 116–141 μm after VUF + LEF treatment.

The homogeneity of grain size is also very important particularly for large-sized billet. Therefore, to evaluate this item, the linear fitting and standard deviation (SD) of grain size distribution are employed. The slope of fitted line reflects the

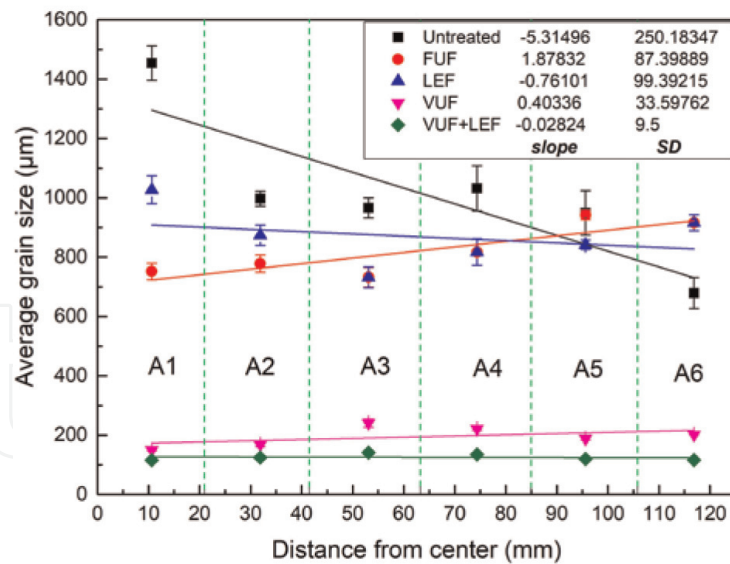


Figure 18.
Grain size distribution of as-cast AZ80 under different external field treatments.

characteristics of grain distribution, and the SD value shows the homogeneity. In case of untreated billet, a negative slope (-5.314) is obtained with the large SD value (250.183), suggesting that the grain size reduces from center to edge and bad homogeneity. After FUF treatment, the slope becomes positive to 1.878, and the SD decreases to 87.399. These results agree with the microstructure observation in **Figure 17**, implying the better refinement caused by FUF in the center part of billet and improvement of homogeneity. The LEF has negative slope and relatively small SD value of -0.761 and 99.392, respectively, which means better grain refinement efficiency in the edge area of billet. The VUF-treated billet has the negative slope similar with the FUF, while the slope is rapidly reduced to 0.403, with the small SD value of 33.598 as well, suggesting the good homogeneity. As for the VUF + LEF-treated billet, the slope and SD are further reduced to -0.028 and 9.5, respectively. Thus, the LEF can help promote the homogeneity.

To better explain and reflect the mechanisms of external field treatment on microstructure evolution of AZ80 alloy, schematic diagrams are given in **Figure 19**. As mentioned above, the cavitation-enhanced heterogeneous nucleation and dendrite fragmentation are two main reasons to refine Mg grains. As shown in **Figure 19(b)**, the ultrasonic cavitation bubble is produced and enlarged because of the negative acoustic pressure, which absorbs heat from melt and generates the local super cooling on the bubble's surface, leading to heterogeneous nucleation on the surface of bubble. The enlarged bubble shrinks and collapses due to the positive acoustic pressure and releases huge impact force to melt, which can fragment the initial crystal nuclei and dendrites. This process is also an effective method to increase the number of nuclei in melt. What is more, it can remove the columnar crystals, and that is why the columnar crystal area disappears in **Figure 17(d)**. These two simultaneously worked mechanisms considerably increase the number of nuclei of α -Mg. Then in the acoustic streaming, the return circulated macroscopic flow in melt (shown in **Figure 19(b)**) carries the nuclei to wider areas, showing the decrease of absolute value of slope and SD compared with the untreated billet. The linear fitting results note that FUF-treated billet has the positive slope of grain size distribution. The sound attenuation should respond for this phenomenon. The acoustic intensity I is inversely related to the propagation distance x , as shown in Eq. (7):

$$I = I_0 e^{-2\alpha x} \quad (7)$$

where α the attenuation coefficient in melt and x the propagation distance. Because of the high attenuation coefficient α value in magnesium melt, the acoustic intensity becomes weak in the edge area of billet, reducing the grain refinement efficiency.

According to the experimental results, the VUF has the better grain refinement ability than FUF. To understand the reason behind this phenomenon, a simple numerical simulation for acoustic pressure distribution in melt is calculated by finite element method. The acoustic pressure distribution is calculated by Eq. (8):

$$\frac{1}{\rho_0 c_0^2} \frac{\partial^2 p}{\partial t^2} - \nabla \cdot \left(\frac{1}{\rho_0} (\nabla p) \right) = 0 \quad (8)$$

where p is the solved acoustic pressure, t is the time, and ρ_0 and c_0 are the melt's density and sound speed in magnesium melt. In this simulation, the solidified Mg billet is not considered. Thus, the physical model only shows the Mg melt during the casting process based on the experimental data. Four boundary conditions are as follows. The melt-air surface is set as the soft wall condition where $P = 0$. The side wall of ultrasonic horn is set as the hard wall condition, where the acoustic wave is totally reflected. The tip surface of ultrasonic horn is set as the acoustic pressure condition, where $p = p_0 \sin(2\pi t(f_0 + \sin(2\pi f_1 t)))$ represents the variable-frequency ultrasonic vibration mode, and the p_0 , f_0 , and f_1 are the amplitude of acoustic pressure, center frequency, and the changing frequency, respectively. The surface of ring and mushy zone are set as the acoustic impedance where the acoustic wave can be absorbed. **Table 3** lists the parameters used in this simulation.

Figure 20 displays the acoustic pressure distribution and corresponding cavitation area. In case of FUF, the maximum negative acoustic pressure is located on the surface of ultrasonic horn with the value of -2.88 MPa. As for VUF, the maximum negative acoustic pressure appears in the area below the tip of horn with the value of -4.58 MPa. Based on the research results of Eskin, the cavitation threshold of light materials is about 1.1 MPa. The results show that the cavitation area of FUF is mainly located in a small area close to the ultrasonic horn but the VUF has larger and wider cavitation area. Therefore, the VUF treatment can both improve the maximum acoustic pressure and the cavitation area. On the one hand, the wider cavitation area can produce more cavitation bubble. On the other hand, higher ultrasonic pressure can bring larger cavitation bubble and promote the acoustic streaming effect. Bigger cavitation bubble means that there is more heat absorbed from the melt which then generates greater degree of supercooling, resulting in increase of number of nuclei, as shown in **Figure 19(c)**. Larger cavitation bubble can also promote the destructive power of impact force released by the collapse of cavitation bubble, improving the dendrite fragmentation effect. The impact force (F_{impact}) is given as [25].

Parameter	Description	Value
p_0	Amplitude acoustic pressure	3.22×10^6
f_0	Center frequency	20 kHz
f_1	Changing frequency	200 Hz
c	Sound speed	4000 m/s
ρ	Density of melt	1780 kg/m ³
Z	Acoustic impedance	4.2×10^7 Pa•s/m

Table 3.
 Parameters used in numerical simulation.

$$F_{impact} = I_{in} \cdot S \cdot e^{-2\alpha x} \cdot \frac{e_1}{c} \quad (9)$$

where I_{in} is the input acoustic intensity outside the bubble; S is the surface of cavitation bubble; α is the attenuation coefficient; x is the transmitted position; e_1 is a unit vector ultrasonic wave associated with the propagation direction; and c is the speed of ultrasound in the magnesium melt. Therefore, the impact force (F_{impact}) has strong relation with the S and I_{in} . On the one hand, the I_{in} is positively relative with the acoustic pressure, according to $I_{in} = p^2/2\rho c$. Thus, the higher acoustic pressure, the larger is I_{in} , suggesting that the VUF can enhance the impact force. On the other hand, higher acoustic pressure also produces the large-sized cavitation bubble, namely, the enlargement of S , leading to the enhancement of impact force (F_{impact}). It is also noticed that the VUF makes the grains more uniform. The improved acoustic streaming effect is responsible for this phenomenon. Due to the fact that the acoustic pressure gradient holds the key to the intensity of acoustic streaming, the higher maximum ultrasonic pressure of VUF can dramatically improve the action sphere of acoustic streaming. Stronger acoustic has better transportation capability and can carry nuclei to further place, promising the homogeneity of billet.

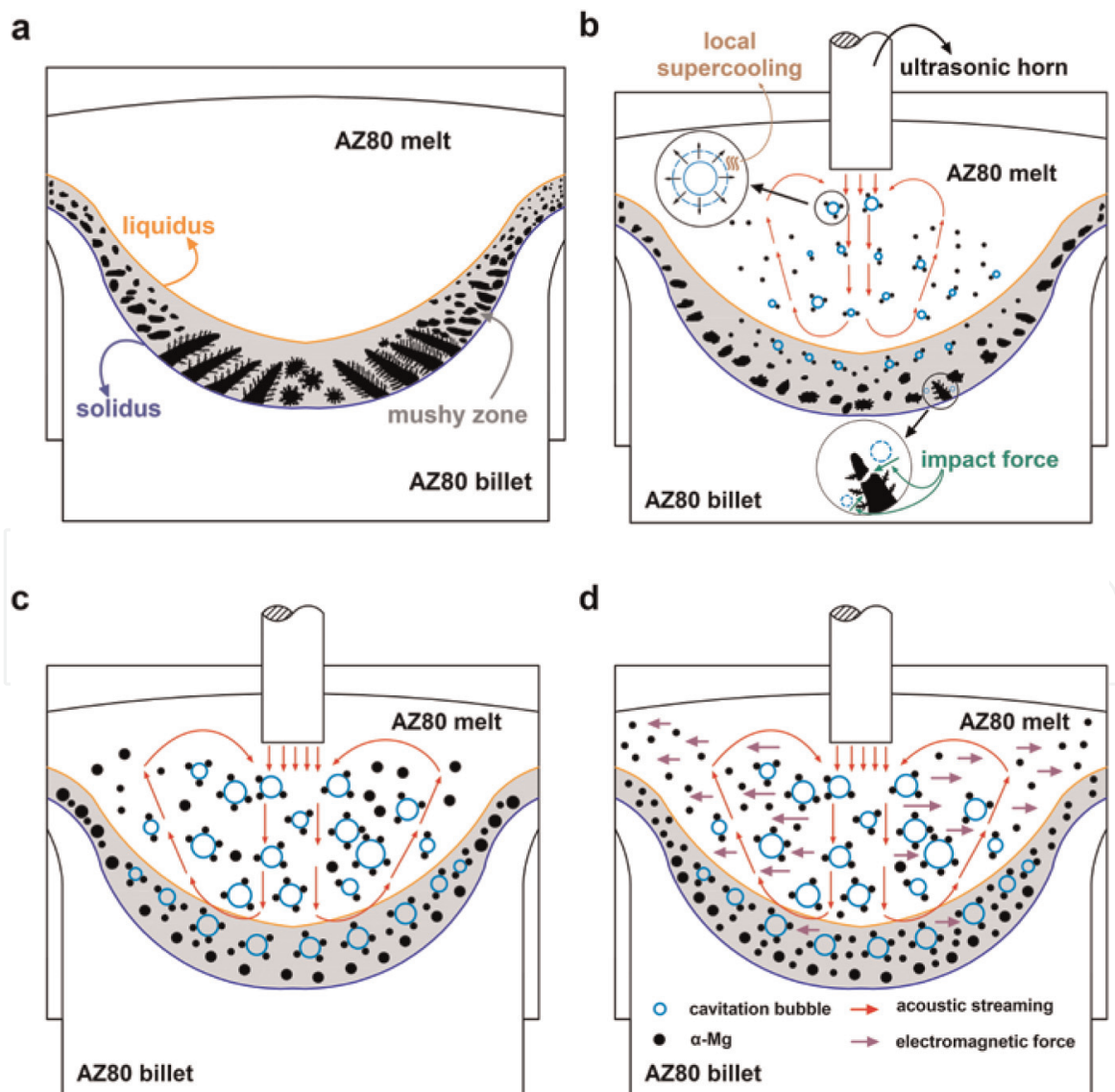


Figure 19. Schematic images of grain refinement associated with different external fields: (a) traditional casting; (b) FUF treatment; (c) VUF treatment; and (d) VUF + LEF treatment.

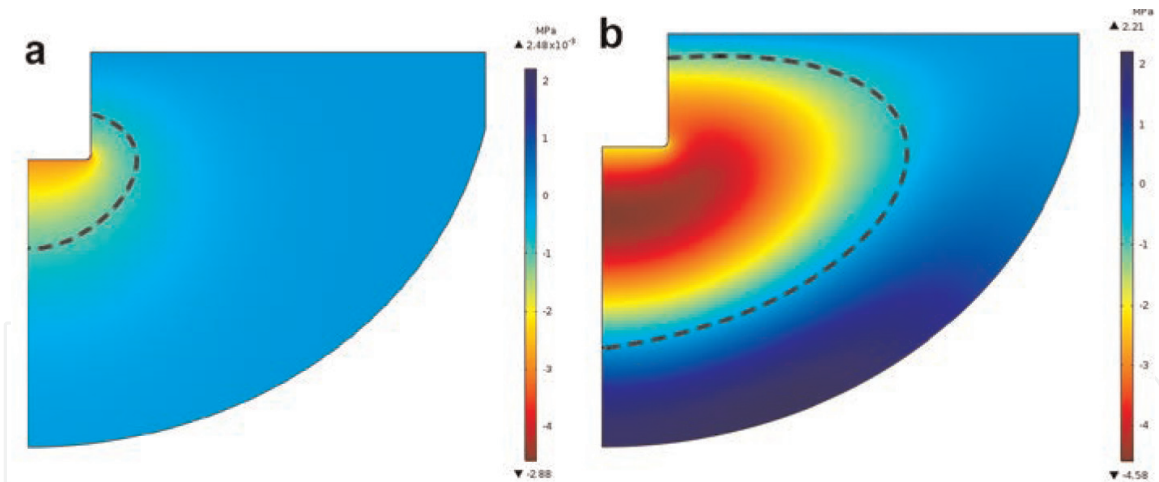


Figure 20.
Acoustic pressure distribution and relevant cavitation area in magnesium melt (a) FUF and (b) VUF.

According to the experimental results, the LEF can also refine the microstructure of AZ80 alloy and improve its homogeneity. In this case, the Lorentz force produced by the electromagnetic field introduces the stirring effect to the melt, which enforces the melt moving from center to edge along the transverse direction. Consequently, the melt with high temperature in center part of melt is carried to the cold mold wall, accelerating the heat and mass transfer. The temperature field becomes uniform, and temperature gradient is reduced as well, which helps in maintaining the nuclei. In addition, the vibrating forces can also break the initial solidified grains formed on the mold wall and then refine the grain.

Now, it is worth to discuss the mechanisms of combination application of VUF and LEF, because it shows the best grain refinement efficiency, with the grain size of 116–141 μm , slope of -0.028 , and SD of 9.5. These two fields have interaction, as show in **Figure 19(d)**. According to the discussion above, the main effect of two fields is different. As for the VUF, increasing the number of nuclei in melt is its uppermost mission. The acoustic streaming is its secondary effect. In case of LEF, accelerating the mass and het transportation is the main effect because it can create a comfortable environment for nuclei. Thus, the VUF generates the large number of nuclei and LEF charge to transport them and make sure they can grow. Finally, the grains become fine with homogeneous distribution.

Author details

Xingrui Chen and Qichi Le*

Key Lab of Electromagnetic Processing of Materials, Ministry of Education, Northeastern University, Shenyang, People's Republic of China

*Address all correspondence to: qichil@mail.neu.edu.cn

IntechOpen

© 2019 The Author(s). Licensee IntechOpen. This chapter is distributed under the terms of the Creative Commons Attribution License (<http://creativecommons.org/licenses/by/3.0/>), which permits unrestricted use, distribution, and reproduction in any medium, provided the original work is properly cited. 

References

- [1] Chen X, Liao Q, Niu Y, Jia Y, Le Q, Ning S, et al. Comparison study of hot deformation behavior and processing map of AZ80 magnesium alloy casted with and without ultrasonic vibration. *Journal of Alloys and Compounds*. 2019; **803**:585-596. DOI: 10.1016/j.jallcom.2019.06.242
- [2] Xu T, Yang Y, Peng X, Song J, Pan F. Overview of advancement and development trend on magnesium alloy. *Journal of Magnesium and Alloys*. September 2019; **7**(3):536-544. DOI: 10.1016/j.jma.2019.08.001
- [3] Chu C, Hu Z, Li X, Yan H, Wu X, Mai Y. Evolution and distribution of Al₂Sm phase in as-extruded AZ61-xSm magnesium alloys during semi-solid isothermal heat-treatment. *Transactions of the Nonferrous Metals Society of China*. 2018; **28**:1311-1320. DOI: 10.1016/S1003-6326(18)64768-5
- [4] Kula A, Tokarski T, Niewczas M. Comparative studies on the structure and properties of rapidly solidified and conventionally cast AM60 magnesium alloys. *Materials Science and Engineering A*. 2019; **759**:346-356. DOI: 10.1016/j.msea.2019.05.044
- [5] Plesset MS, Prosperetti A. Bubble dynamics and cavitation. *Annual Review of Fluid Mechanics*. 1977; **9**: 145-185
- [6] Anderson PW. Absence of diffusion in certain random lattices. *Physics Review*. 1958; **109**:1492-1505. DOI: 10.1103/PhysRev.109.1492
- [7] Liu X, Zhang J, Li H, Le Q, Zhang Z, Hu W, et al. Electrical resistivity behaviors of liquid Pb-Sn binary alloy in the presence of ultrasonic field. *Ultrasonics*. 2015; **55**:6-9. DOI: 10.1016/j.ultras.2014.07.008
- [8] Liu X, Zhang Z, Hu W, Le Q, Bao L, Cui J, et al. Study on hydrogen removal of AZ91 alloys using ultrasonic argon degassing process. *Ultrasonics Sonochemistry*. 2015; **26**:73-80. DOI: 10.1016/j.ultsonch.2014.12.015
- [9] Liu X, Zhang C, Zhang Z, Xue J, Le Q. The role of ultrasound in hydrogen removal and microstructure refinement by ultrasonic argon degassing process. *Ultrasonics Sonochemistry*. 2017; **38**:455-462. DOI: 10.1016/j.ultsonch.2017.03.041
- [10] Liu X, Xue J, Zhao Q, Le Q, Zhang Z. Effects of radiator shapes on the bubble diving and dispersion of ultrasonic argon process. *Ultrasonics Sonochemistry*. 2018; **41**:600-607. DOI: 10.1016/j.ultsonch.2017.10.026
- [11] Sigworth GK, Engh TA. Chemical and kinetic factors related to hydrogen removal from aluminum[J]. *Metallurgical Transactions B*. 1982; **13** (3):447-460
- [12] Papamantellos D, Lange KW, Okohira K, Schenck H. A mathematical approach for the mass transfer between liquid steel and an ascending bubble. *Metallurgical and Materials Transactions B: Process Metallurgy and Materials Processing Science*. 1971; **2**: 3135-3144. DOI: 10.1007/BF02814966
- [13] Zhang ZQ, Le QC, Cui JZ. Effect of Ultrasonic Treatment on Microstructures of Mg-Ca Binary Alloy [C]//Advanced Materials Research. Trans Tech Publications; 2010; **139**: 677-680
- [14] Shao Z, Le Q, Zhang Z, et al. Effect of ultrasonic power on grain refinement and purification processing of AZ80 alloy by ultrasonic treatment[J]. *Metals and Materials International*. 2012; **18**(2): 209-215
- [15] Eskin GI. Principles of ultrasonic treatment: Application for light alloys

- melts. *Advanced Performance Materials*. 1997;**4**:223-232. DOI: 10.1023/A:1008603815525.
- [16] Hunt JD, Jackson KA. Nucleation of solid in an undercooled liquid by cavitation. *Journal of Applied Physics*. 1966;**37**:254-257. DOI: 10.1063/1.1707821
- [17] Jin J, Ma H, Wang K, Yagoub AE-GA, Owusu J, Qu W, et al. Effects of multi-frequency power ultrasound on the enzymolysis and structural characteristics of corn gluten meal. *Ultrasonics Sonochemistry*. 2015;**24**: 55-64. DOI: 10.1016/j.ultsonch.2014.12.013
- [18] Shankar PM, Chapelon JY, Newhouse VL. Fluid pressure measurement using bubbles insonified by two frequencies. *Ultrasonics*. 1986;**24**:333-336. DOI: 10.1016/0041-624X(86)90004-1
- [19] Phelps AD, Ramble DG, Leighton TG. The use of a combination frequency technique to measure the surf zone bubble population[J]. *The Journal of the Acoustical Society of America*. 1997;**101** (4):1981-1989
- [20] Chen X, Ning F, Hou J, Le Q, Tang Y. Dual-frequency ultrasonic treatment on microstructure and mechanical properties of ZK60 magnesium alloy. *Ultrasonics Sonochemistry*. 2018;**40**:433-441. DOI: 10.1016/j.ultsonch.2017.07.027
- [21] Jia Y, Chen X, Le Q, Wang H, Jia W. Numerical study on action of HMF, PMF, DHMF, and DPMF on molten metal during electromagnetic casting. *International Journal of Advanced Manufacturing Technology*. 2019;**103**: 201-217. DOI: 10.1007/s00170-019-03501-y
- [22] Chen X, Le Q, Wang X, Liao Q, Chu C. Variable-frequency ultrasonic treatment on microstructure and mechanical properties of ZK60 alloy during large diameter semi-continuous casting. *Metals*. 2017;**7**:173. DOI: 10.3390/met7050173
- [23] Chen X, Jia Y, Liao Q, Jia W, Le Q, Ning S, et al. The simultaneous application of variable frequency ultrasonic and low frequency electromagnetic fields in semi continuous casting of AZ80 magnesium alloy. *Journal of Alloys and Compounds*. 2019;**774**:710-720. DOI: 10.1016/j.jallcom.2018.09.300
- [24] Jia Y, Wang H, Le Q. Transient coupling simulation of multi-physical field during pulse electromagnetic direct-chill casting of AZ80 magnesium alloy. *International Journal of Heat and Mass Transfer*. 2019;**143**:118524. DOI: 10.1016/j.ijheatmasstransfer.2019.118524
- [25] Liu Q, Zhai Q, Qi F, Zhang Y. Effects of power ultrasonic treatment on microstructure and mechanical properties of T10 steel. *Materials Letters*. 2007;**61**:2422-2425. DOI: 10.1016/j.matlet.2006.09.027